Inverse design of colored daytime radiative coolers using deep neural networks

Harit Keawmuang [a,1], Trevon Badloe [b,1], Chihun Lee [a], Junkyeong Park [a], Junsuk Rho [a,c,d,e,*]

[a] *Department of Mechanical Engineering, Pohang University of Science and Technology (POSTECH), Pohang, 37673, Republic of Korea*
[b] *Graduate School of Artificial Intelligence, Pohang University of Science and Technology (POSTECH), Pohang, 37673, Republic of Korea*
[c] *Department of Chemical Engineering, Pohang University of Science and Technology (POSTECH), Pohang, 37673, Republic of Korea*
[d] *Department of Electrical Engineering, Pohang University of Science and Technology (POSTECH), Pohang, 37673, Republic of Korea*
[e] *POSCO-POSTECH-RIST Convergence Research Center for Flat Optics and Metaphotonics, Pohang, 37673, Republic of Korea*

ARTICLE INFO

ABSTRACT

Passive daytime radiative cooling is an eco-friendly and cost-efficient cooling strategy that is achieved by selectively reflecting the solar irradiance and emitting heat to cold background of the universe through the atmospheric window (AW) at infrared wavelengths. The daytime radiative coolers traditionally exhibit a grey or white color due to the requirement of high solar irradiance reflectance. Here, we present a colored daytime radiative cooler (CDRC) that has high reflectance in the NIR, high emissivity in the AW, and the capability to generate subtractive primary colors based on Fabry-Pérot interference using metal-insulator-metal (MIM) structures. The structural parameters of the MIM multilayers are inversely designed using tandem neural networks to achieve cooling powers of 11.2–38.2 W/m^2 with on-demand color generation. The proposed CDRCs have potential to be used for cooling thermal sensitive electronic and optoelectronic devices and aesthetic applications.

1. Introduction

The problem of global warming is causing a significantly increased demand for cooling in cars, buildings, and households, leading to a higher amount of energy consumption by conventional cooling methods [1,2]. Hence, daytime radiative cooling has gained huge interest over recent years for its ability to reach sub-ambient temperatures without any energy input [3–12]. The concept of daytime radiative cooling is to use outer space as a large heat sink to release heat through the atmospheric window (AW), where the atmosphere of the Earth is highly transparent between the wavelength range of 8–13 μm, and simultaneously reflect the solar irradiation from the ultra-violet (UV) to the near-infrared (NIR) region [6]. The ideal optical properties of daytime radiative cooling are shown in Fig. 1(a). There are various applications that daytime radiative cooling has been implemented for such as cooling for electronic devices [13,14], photovoltaics [15,16], and transparent energy-saving windows for cars or buildings [17,18].

One drawback of such daytime radiative coolers is that by reflecting all of the solar illumination means that the surface will necessarily

appear white. However, research has been undertaken to simultaneously present vivid colors along with the desirable cooling effect to develop colored daytime radiative cooler (CDRC) [19]. The additional color can be used for safety and aesthetic purposes such as decoration for windows, cars, and other objects. Numerous design approaches for CDRC have been demonstrated, for instance, Son et al. employed nanocrystals to realize color generation using the effect of photoluminescence quantum yields, in which some of the photons and thermal energy will be absorbed and subsequently emit light in the visible regime [20]. Meanwhile, Yoon et al. generated colored daytime radiative cooling by fabricating Cu-based quantum dots using the same photoluminescent effect [21]. However, the absorption of the ultraviolet photons of the photoluminescent effect might reduce the cooling performance of the CDRC. Additionally, Min et al. [22] presented CDRCs based on photoluminescence, demonstrating high cooling performance, however it is important to note that the proposed delta-function-like emission and excitation required are difficult to realize in practice. Another approach to create CDRC is to use dielectric resonant structures, for example, CDRC based on the optical Tamm resonance [23], and Fabry-Pérot

interference using metal-insulator-metal (MIM) structures [24,25]. The films were designed using conventional parametric sweeping methods to study the effect of the metal and cavity thickness on the color generation that can investigate only one candidate material at a time. Various optimization methods have been adopted to assist the color generation of nanophotonic structures such as employing genetic algorithm to optimize a broadband multilayer film [26,27]. However, the iterative process of the optimization must be repeated if the desired color is changed, as only a single figure of merit can be defined for each optimization run. Recently, there has been a significant attention toward an inverse design in photonics based on artificial intelligence (AI) that is able to discover new designs beyond training datasets without the iterative means and limited boundaries [28–32]. Guan et al. [33] also developed an on-demand transmissive CDRC by employing machine learning-based inverse design to predict colors from the structural parameters of pixelated nanocavities. Despite being able to predict different colors from the parametric structure, the cooling power is not taken into consideration. This means that the model only gives the output colors without considering the subsequent cooling power. Furthermore, transmission type radiative coolers have a distinct drawback in that most of the energy radiated by the sun will pass through, leading to increased heating.

In this work, we adopt a machine learning-based inverse design method to develop a CDRC for on-demand colors while considering the effect of the structures and cavity materials on both color saturation and cooling power. We design and train deep neural networks (DNNs) using the concept of tandem neural networks [29,33]. The tandem architecture is specifically designed to solve the one-to-many problem that commonly occurs in the nanophotonic structure design, where multiple structures can produce the same spectral response, making the DNNs struggle to converge. By first training a forward neural network (FNN) and then connecting an inverse neural network (INN) to the well-trained FNN, such convergence problems are alleviated, and the fully trained INN can be used directly for inverse design. This inverse design method can be used to quickly uncover CDRC designs that take both the reflected color and cooling power into account.

There are two main parts that make up our CDRC, namely, a selective emitter (SE) and a MIM cavity. The SE serves to selectively produce a high emissivity in the AW to radiate energy away, while the MIM structure is chosen for the color generation due to producing narrow spectral resonances and high reflectivity across the rest of the solar irradiance spectrum [25]. The schematic of the reflective CDRC is shown in Fig. 1(b). A high emissivity material is used to serve as the SE part.

Then, the cavity structure is developed by using the tandem neural networks. After training, the network will be able to provide the best parametric structures and cavity materials for target colors with a balance level of color saturation and cooling power.

2. Results and discussion

2.1. Concept and design

The purpose of a radiative cooler is to provide a cooling power that realizes sub-ambient temperatures. In order to achieve this, the following ideal optical responses of the cooler must be satisfied (see Fig. 1(a)). First, the cooler requires to have a high emissivity in the AW ($8 < \lambda < 13$ μm) to emit thermal energy. Also, it is worth noting that in the mid-infrared (MIR) wavelength range, outside AW, there is a significant downward radiation from the atmosphere that is absorbed by the cooler. Hence, the emissivity of the cooler outside AW should be low to reduce such absorption. Second, to prevent the cooler from gaining heat from the sun, it should have maximal reflectance in the UV to NIR wavelength range. For CDRC however, some wavelengths in the visible region must be present for a color to be demonstrated. Multilayer MIM structures provide an ideal solution for reflective color generation, due to their high Q-factors and ease of fabrication. Therefore, here, we combine a SE and MIM cavity to design a CDRC. The SE selectively emits heat through the AW and the MIM cavity generates the reflected colors while maximizing the reflectance at other visible and NIR wavelengths. We use polydimethylsiloxane (PDMS) to serve as the SE as it has been widely reported to provide a high emissivity across the AW region [17]. For designing the photonic structure to control color, we use a deep learning-based inverse design method to effectively create colors while maximizing the cooling power by designing the structural parameters and insulator material of the MIM. The MIM produces an absorption dip in the reflected spectrum, which then displays subtractive primary colors, cyan, magenta, and yellow (CMY). Multiple colors can be realized through the combination of these subtractive primary colors, while the MIM structure also serves to reflect the solar spectrum in NIR.

The cooling power of the CDRC can be calculated from the heat absorbed from the solar irradiance, atmospheric radiation, and non-radiative heat transfers, namely, convection and conduction, and how much thermal energy is emitted through the AW. A thermal equilibrium equation consisting of these four thermal fluxes can be defined as follows [9]:

$$P_{cool}(T, T_{amb}) = P_{rad}(T) - P_{sun} - P_{atm}(T_{amb}) - P_{cc}(T, T_{amb}) \qquad (1)$$
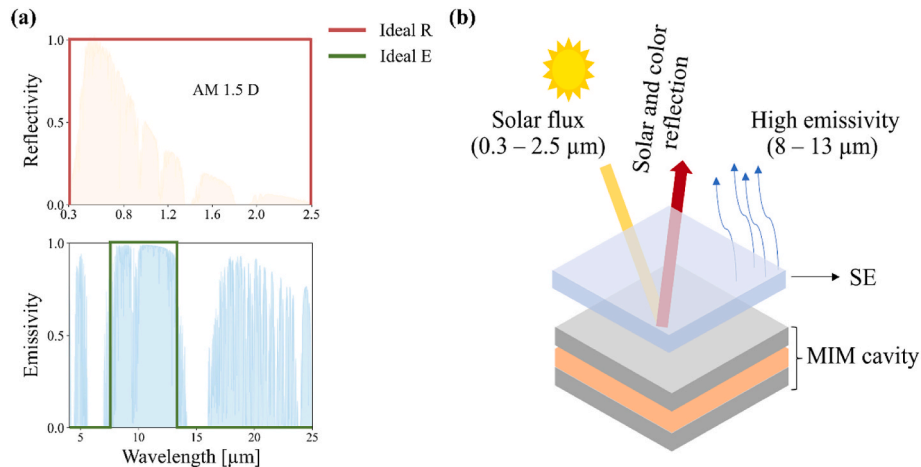

Fig. 1. (a) The ideal optical responses for daytime radiative cooling with the solar spectrum (orange shaded area) and the atmosphere transmission spectrum (blue shaded area). AM 1.5 D denotes the standardized solar spectrum for direct sunlight at sea level with an air mass of 1.5. Ideal R represents an ideal reflectivity of the cooler in solar range. Ideal E represents an ideal emissivity of the cooler in mid-infrared region. (b) Schematic of the working principle of a colored radiative cooler made up of a selective emitter (SE) and metal-insulator-metal (MIM) Fabry-Pérot cavity.

Where,

$$P_{sun} = \int \varepsilon(\lambda) I_{solar}(\lambda) d\lambda \qquad (2)$$

is the thermal flux by solar irradiance,

$$P_{rad}(T) = \int \int_0^\infty I_{BB}(T, \lambda) \varepsilon(\lambda, \Theta) d\lambda \cos\Theta d\Omega \qquad (3)$$

is the power flux radiate from the cooler,

$$P_{atm}(T_{amb}) = \int \int_0^\infty I_{BB}(T_{amb}, \lambda) \varepsilon(\lambda, \Theta) \varepsilon_{atm}(\lambda, \Theta) d\lambda \cos\Theta d\Omega \qquad (4)$$

is the power flux absorbed by the atmospheric temperature,

$$P_{cc}(T, T_{amb}) = h_{cc}(T_{amb} - T) \qquad (5)$$

is the nonradiative heat transfers.

Here, $\varepsilon(\lambda)$ is spectral emissivity at λ and I_{solar} is spectral solar transmittance. Θ is the polar angle, we use $\Theta = 0$ as we consider the normal incidence case. By Kirchhoff's law [34], $\varepsilon(\lambda, \Theta)$ is equal to the absorptivity at the same wavelength and polar angle. Also, $I_{BB}(T, \lambda)$ represents the spectral radiance density of a blackbody. T_{amb} expresses the ambient temperature, $\varepsilon_{atm}(\lambda, \Theta) = 1 - t^{(\lambda)1/\cos\Theta} d\Omega$ is the atmospheric emissivity. Lastly, h_{cc} is the heat transfer coefficient.

2.2. Training of the deep neural networks

To create the dataset required to train the DNNs, we perform a series of rigorous coupled-wave analysis (RCWA) simulations. For the MIM materials, we choose Ag as the top and bottom metals, and four
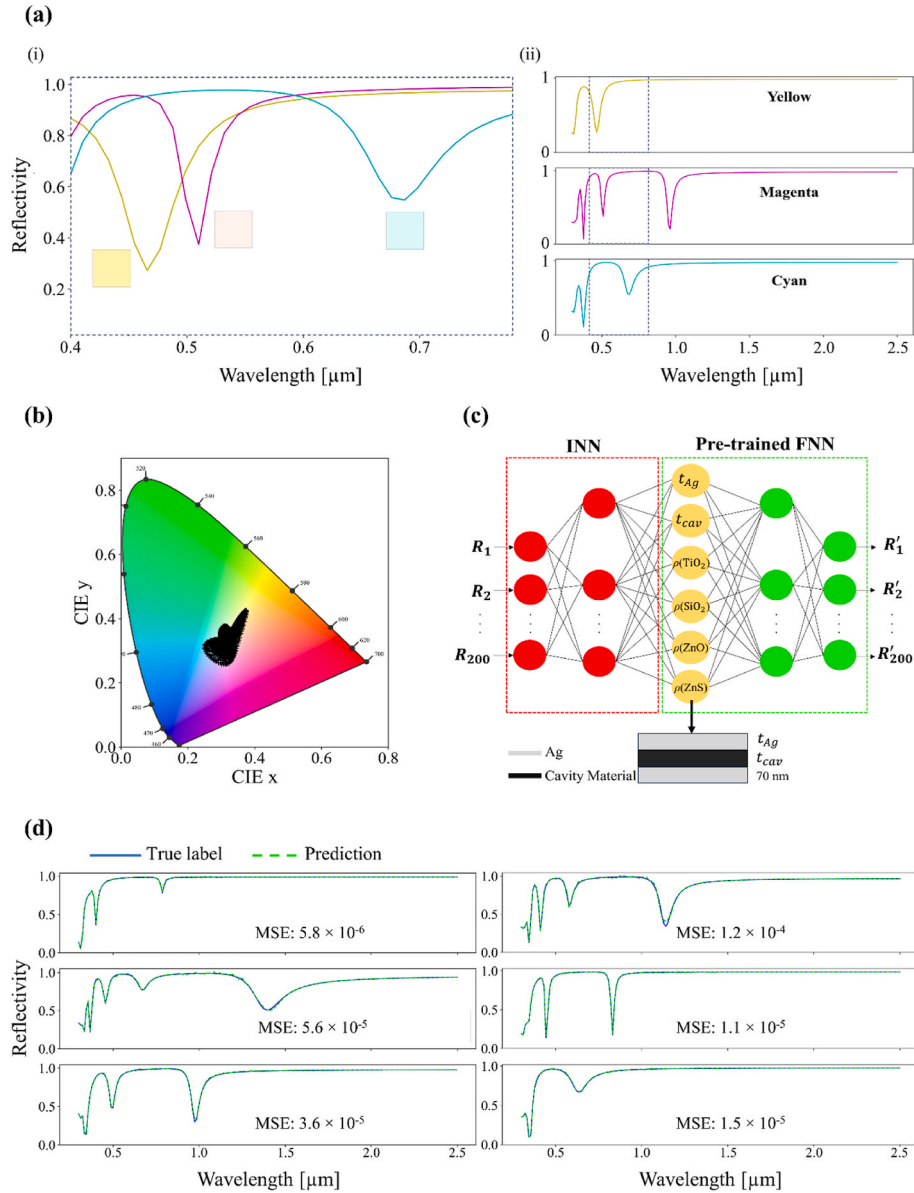

Fig. 2. (a) Examples of the reflectivity spectra producing primary subtractive CMY colors from the training samples at (i) visible and (ii) UV to NIR wavelengths. (b) Colors of the generated dataset plotted on the CIE 1931 chromaticity diagram. (c) Schematic of the tandem neural network architecture. (d) Examples of predicted spectra from the trained FNN from unseen test data.

candidate materials are chosen as the insulator material. For the bottom layer material, it plays as a light reflector which other metals (e.g., aluminum or gold) can also be used instead of Ag. However, the reflected color would be different accordingly due to the difference in reflectivity of the metal. The cavity materials are TiO$_2$, ZnO, ZnS, and SiO$_2$, which have high refractive indices and low extinction coefficients at visible wavelengths. The simulations are performed by fixing the thickness of the bottom Ag to be 70 nm and varying the thickness of top Ag (t_{Ag}) from 0 to 98 nm and cavity (t_{cav}) in the range of 40–236 nm in each candidate materials. A total of 10,000 simulations are conducted with 200 values of each spectral data in the wavelength range of 0.3–2.5 μm. As such, it is worth emphasizing that the predictive capability of our DNNs is optimized specifically to predict the optical response within the solar irradiance spectrum, rather than extending to the AW region. However, it is notable that DNNs can be trained to predict the optical response in the different wavelength regimes at will by creating the required dataset and has been proven in the NIR [35] and MIR [28,35, 36]. Dips are observed in the reflectance spectra in the visible wavelength range which show that the structure produces colors. Examples of the reflectance spectra creating CMY colors can be seen in Fig. 2(a). For the spectra to color conversion calculations, see Supporting Information. In addition to generating colors, the MIM multilayers can also effectively reflect the solar irradiance at NIR wavelengths, leading to higher cooling powers. However, undesired second order resonances can also be observed at NIR wavelengths for some structures. The colors from the dataset are plotted in the CIE-1931 standard observer in Fig. 2(b).

Tandem neural networks are used to perform the inverse design of the CDRC. The tandem architecture consists of a pre-trained FNN and an INN. The FNN takes t_{Ag}, t_{cav}, and cavity materials as input parameters, and gives the reflectance spectra as the output. The INN, on the other hand, receives the spectral data as the input and provides the structural parameters as the output. After training the FNN, the INN is then connected in tandem and trained, while the weights and biases of the FNN are frozen. A schematic of this architecture is shown in Fig. 2(c). The inputs of the model are the simulated reflectivity from $\lambda = 0.3$–2.5 μm, $R = [R_1, R_2, ..., R_{200}]$, and the output reflectivity $R' = [R'_1, R'_2, ..., R'_{200}]$ given by the FNN. We first train the FNN using 6 input parameters, t_{Ag}, t_{cav}, and 4 one-hot encoded cavity materials. The outputs are 200 values of reflection spectra. By the optimization of hyperparameters, we construct a FNN that consists of 4 hidden layers. The first two layers have 250 neurons, and the last two layers contain 450 neurons. The root mean squared propagation (RMSprop) is adopted as the optimizer with a learning rate of 5×10^{-5} and batch size of 32, while rectified linear unit (ReLU) is used as the activation function. The mean square error (MSE) loss is used to determine loss between true labels and predictions during the training. After the completion of training, the performance of the FNN is evaluated by predicting the spectra of unseen data in the test dataset, and comparing it with the ground truth reflectivity from the simulation. Some examples of the spectra predicted by the FNN from the test dataset are presented in Fig. 2(d). It can be seen that the predictions of the model accurately match the ground truth reflectivity data with a minimum MSE loss as low as 5.8×10^{-6}. The average loss of the test dataset is 3.8×10^{-5}, which shows that the model performs well at predicting the spectra of the unseen data.

The INN is then connected to the trained FNN. The INN takes a desired spectral response as the input, and gives outputs (Y) that relate to the thickness of the layers and probability of each material as follows:

$$Y = [Y_1, Y_2, Y_3, Y_4, Y_5, Y_6] = [t_{Ag}, t_{cav}, \rho(TiO_2), \rho(SiO_2), \rho(ZnO), \rho(ZnS)]$$

(6)

The INN shares the same architecture as the FNN, i.e., it consists of the same numbers of layers and neurons per each layer with ReLU activation function in the hidden layers. For the output layers, linear and softmax activation functions are used for the thickness and material probability outputs, respectively. An adaptive moment estimation

(Adam) optimization algorithm is used as the optimizer with a scheduling learning rate of 5×10^{-4} in the first 500 epochs and 5×10^{-5} in the last 500 epochs according to the hyperparameters optimization. Weight decay of 2×10^{-5} is also applied to the inverse model to prevent overfitting. Again, MSE loss is applied as the loss function as the model is trained to reduce loss between the input spectra and predicted spectra from the FNN. See Fig. S2 for the training and validation loss curves for the FNN and INN. After the training, the unseen test dataset is used to evaluate the performance. An average MSE loss of 2.5×10^{-3} is calculated for the test dataset. To confirm that the model is providing designs that give the desired spectra, we performed RCWA simulations on the inverse designed parameters from the INN. Comparisons of the 'desired reflectivity' i.e. the test dataset reflectivity and the reflectivity obtained from the inverse designed structures, which we refer to as the 'designed reflectivity' are shown in Fig. 3. We can confirm that the tandem network has not simply memorized the training data, as the original and suggested structures are completely different, with different materials and thicknesses, however, the designed spectra are closely matched.

2.3. Inverse design of the CDRC

To perform the inverse design of CDRC using the successfully trained inverse model, we hand-draw reflectivity targets (R_{target}) using Lorentzian-shaped functions as defined by Eq. (7):

$$R_{target} = 1 - \frac{1 - A}{1 + \left(\frac{\lambda - \lambda_{dip}}{w}\right)^2},$$

(7)

where A is the amplitude of the dip, λ_{dip} is the dip position, and w is the width of the dip. The target spectrum is designed to have a reflection dip in VIS to display colors, and possess a unity reflectivity in UV and NIR region to minimize solar thermal flux absorption. The target reflectivity is designed to change λ_{dip} along the VIS region to obtain different primary colors, where λ_{dip} of (a) 0.46 μm (yellow), (b) 0.58 μm (magenta), and (c) 0.65 μm (cyan) are presented. The designed structures are listed in Table 1. The cavity material with the highest probability is chosen as the designed material. Following the literature [17], a 50 μm thick-layer of PDMS is then placed on top of the MIM cavity to selectively emit in the AW.

For each design, we plot the target, RCWA simulation from the inverse designed structure, and the FNN predicted spectrum in Fig. 4(a–c). The reflected color of the cooler is defined by the location of λ_{dip}, so we calculate the percentage error of the λ_{dip} location between the target and inverse designed simulations using Eq. (8).

$$\lambda_{dip}\ [\%\ Error] = \frac{|\lambda_{dip,target} - \lambda_{dip,simulation}|}{\lambda_{dip,target}} \times 100\%$$

(8)

The obtained percentage error calculations of λ_{dip} are (a) 2.43%, (b) 9.59%, and (c) 6.76%. It can be seen that the minimum λ_{dip} error of the designed structure spectra is as low as 2.43%, and all of the inverse designed spectra accounted for less than a 10% error in λ_{dip}. This results in colors that match well with the designed CMY colors, however, due to the slight error in λ_{dip}, the inverse designed colors display slightly different tones. Furthermore, importantly for radiative cooling performance, all of the inverse designed spectra feature near-unity reflectance across NIR wavelengths.

Since no sunlight is allowed to transmit through the CDRC, the absorption is calculated by subtracting the obtained reflectivity from unity to calculate P_{sun} in order to quantitatively compare the different colored CDRCs. The calculated P_{sun} for each color is presented in Table 2. The P_{sun} of the hand-drawn target spectra for the CDRC is calculated to be 30.0, 47.1, and 31.1 W/m^2 for the yellow, magenta, and cyan coolers, respectively. These are the ideal cases however, perfect unity reflectivity except for the color producing dip in the visible region. However, in reality, due to absorption at UV wavelengths, and dips that have slightly
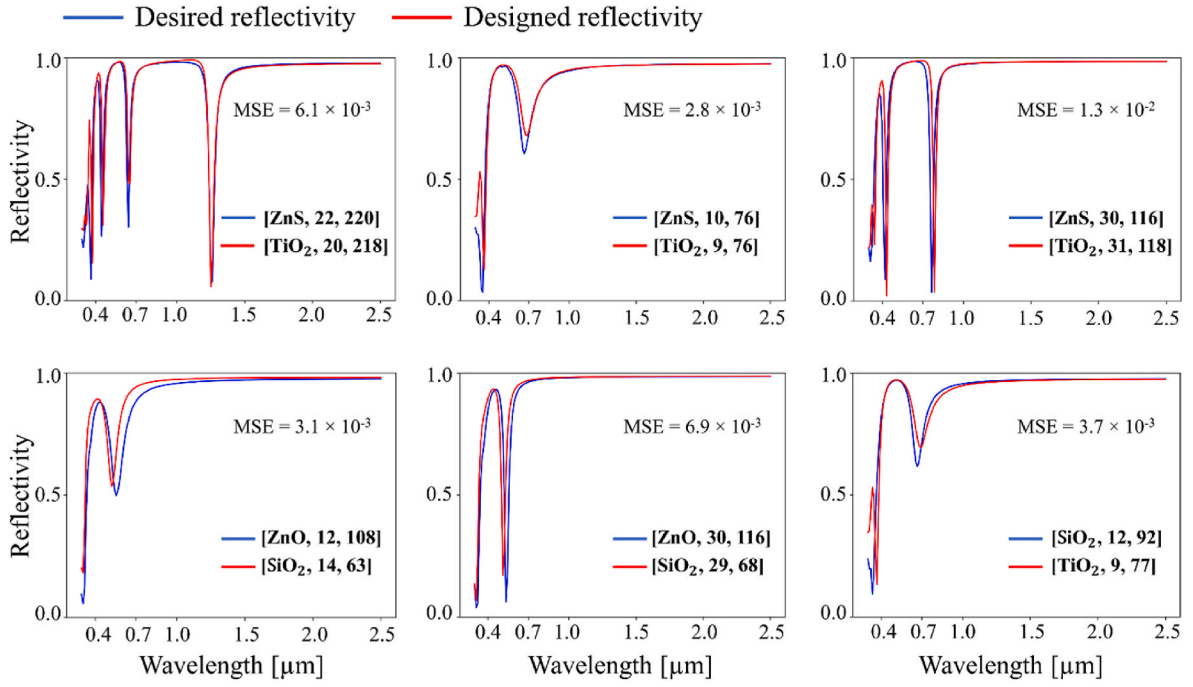
Fig. 3. Comparison between the desired reflectivity from the test dataset and the designed reflectivity from the inverse designed structures from the INN. The text box indicates the inverse design parameters of [cavity material, t_{Ag} (nm), t_{cav} (nm)].

Table 1
Parameters of the inverse designed structures.

λ_{dip} [µm]	t_{Ag} [nm]	t_{cav} [nm]	$\rho(TiO_2)$	$\rho(SiO_2)$	$\rho(ZnO)$	$\rho(ZnS)$
0.46	14	49	0.10	0.72	0.01	0.17
0.58	32	56	0.48	0.15	0.01	0.37
0.65	22	89	0.06	0.72	0.01	0.21

wider responses, the inverse designed CDRCs show slightly higher P_{sun} of 101.4, 74.5, and 88.6 W/m^2 for yellow, magenta, and cyan coolers, respectively. To further analyze the cooling power of the designed CDRCs, the emissivity across the wavelength range of 0.3–15 µm has to be considered according to Eq. (1). See Fig. S3 for the emissivity in the UV, VIS, NIR, and AW regions of the designed CDRCs. Notably, the performance of SE could be optimized to enhance spectral emissivity in
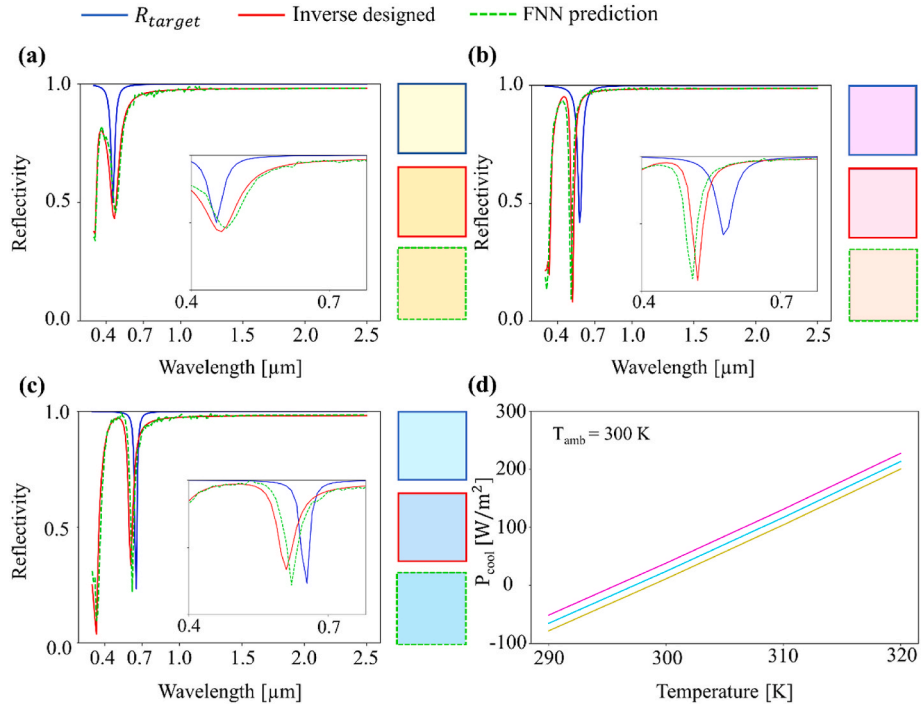

Fig. 4. The reflection spectra for λ_{dip} of (a) 0.46 µm, (b) 0.58 µm, and (c) 0.65 µm and the corresponding colors from each cooler with the blue solid line represents the target cooler, red solid line is inverse designed simulation, and green dotted line is FNN prediction. (d) Calculated P_{cool} of the inverse designed CDRCs with λ_{dip} = 0.46 (yellow), 0.58 (magenta), 0.65 (cyan) µm.

Table 2
P_{sun} of the target, inverse designed, and FNN spectra.

	λ_{dip} [μm]	P_{sun} [W/m^2]
Target	0.46	30.0
	0.58	47.1
	0.65	31.1
Inverse designed	0.46	101.4
	0.58	74.5
	0.65	88.6
FNN	0.46	102.3
	0.58	76.1
	0.65	89.7

the AW range [33]. The net cooling power of the inverse designed CDRCs are plotted in Fig. 4(d) using $h_{cc} = 6$ Wm^{-2}k^{-1}, $T_{amb} = 300$ K, with T varying from 290 to 320 K. See Fig. S4 for the power fluxes' calculation of the inverse designed CDRCs. It is worth noting that P_{rad}, P_{atm}, and P_{cc} do not present any remarkable differences between the CMY coolers since Fig. S3 shows that all the designed coolers have very similar emissivity spectra across AW. This underscores the significance of the differences of P_{sun} among the designed coolers, as it greatly influences the cooling performance of the coolers. The maximum P_{cool} at the ambient temperature is generated by the magenta CDRC, which accounts for 38.2 W/m^2. However, the net cooling power of yellow and cyan coolers are 11.2 and 24.1 W/m^2 at T_{amb}, respectively, which are lower than that of the magenta cooler since they exhibit the higher P_{sun}. It is worth noting that, according to Eq. (1), Eq. (4), and Eq. (5), the change of T_{amb} will significantly influence the cooling power of the cooler. As T_{amb} gets higher, the cooler absorbs greater power flux from the ambient temperature, resulting in minimizing of cooling power. Also, we can see that P_{cool} of the CDRCs increases significantly as the cooler temperature gets higher since conduction and convection play as additional channels for heat releasing along with P_{rad} because of $T > T_{amb}$. The cooling power of the CDRCs should be also investigated by considering non-radiative heat exchange of conduction and convection to the surroundings, various values of h_{cc} (4, 6, 8, and 10 Wm^{-2}k^{-1}) are used for the cooling power calculation to represent practical cases of various environment conditions (see Supporting Information 6). For these values of heat transfer coefficients, the yellow, magenta, and cyan coolers show the temperature reduction up to 1.7 K, 5.5 K, and 3.5 K, respectively, below the ambient temperature of 300 K. Please note that the aforementioned cooling power is obtained under normal emissivity conditions. For a comprehensive understanding of the impact of the angular emissivity on cooling power, please refer to Supporting Information 7. Since the cooling power of the coolers are non-zero, this implies that the coolers material is not in thermal equilibrium and experience dynamic temperature changes. So, we conduct the time-domain outdoor simulation to observe the temperature reduction of the coolers with respect to the actual ambient temperature and time-varying solar irradiance (see Supporting Information 8). The proposed radiative coolers could be fabricated using spin-coating process for PDMS materials [17,18]. Due to the uncertainty in the thickness of the spin-coating process, the corresponding emissivity spectra in AW would be different and therefore cooling power of the coolers might be changed accordingly. However, our designed coolers can still maintain the same cooling performance even considering the uncertainty in thickness of the spin-coating (see Supporting Information 9). Moreover, deposition techniques (e.g., electron-beam evaporation) could be employed for the MIM layers fabrication [17,18]. From previous studies on multilayer radiative cooling [3,17], our typical substrate size could be 4 inches in diameter which has been proven to be feasible for fabrication and to maintain cooling performance of the cooler. Also, there is no influence on the DNNs prediction of the optical responses by a substrate such as SiO$_2$ that exhibits radiative cooling performance (refer to Supporting Information 10).

3. Conclusion

In summary, we demonstrated the inverse design of colored daytime radiative cooler structures using machine learning. The CDRCs consist of an SE and an inverse designed MIM multilayer cavity to reflect NIR radiation and generate subtractive colors. The tandem neural network architecture is adopted to perform an inverse design of the structural parameters of the thickness and materials of the MIM structure. We successfully inverse design the MIM structures to generate a high purity CMY colors for hand-drawn target spectra. The near unity reflection at NIR wavelengths contribute to minimizing the solar power absorbed by the CDRCs. Moreover, the coolers exhibit a high emissivity across the AW region, and they are be able to achieve the cooling power of 11.2, 38.2, and 24.1 W/m^2 for yellow, magenta, and cyan coolers, respectively. P_{cool} could be potentially improved further by optimizing the selective spectral emissivity in the AW up to its theoretical limit [37]. The CDRCs designed here could be simply fabricated using spin-coating methods and different colors could be designed on demand with the same well-trained DNNs. We envision that such inverse designed CDRCs can be used on wearable electronic devices and other applications where aesthetically pleasing colors are required alongside cooling performance.

We note that our DNN is limited to demonstrating predictive capabilities within the UV-NIR range. While this is enough to provide on-demand inverse designs of desired reflection spectra for CDRCs, the complete design of a CDRC requires the prediction of optical properties in the AW region as well. This limitation could be overcome by training the DNNs with additional data that is specifically tailored to the required wavelength regime, or with a separate supplementary optimization process using methods such as genetic algorithms. Furthermore, the DNNs trained in this work operate effectively only for the specific material system that is it trained for, i.e., four candidate cavity materials sandwiched between layers of silver, therefore, any change from this system could lead to a loss of functionality for inverse design of CDRCs. We envision future work on expanding the applicability of DNNs to any arbitrary materials by incorporating larger datasets with represent a broader range of materials, or through the direct implementation of the complex refractive index of materials, thereby enhancing the potential for practical applications across diverse material combinations.

Data availability

Data will be made available on request.

CRediT authorship contribution statement

Harit Keawmuang: Writing – original draft, Visualization, Methodology, Investigation, Formal analysis, Data curation. **Trevon Badloe:** Writing – original draft, Methodology, Investigation, Formal analysis, Data curation. **Chihun Lee:** Investigation, Formal analysis. **Junkyeong**

Park: Investigation, Formal analysis. **Junsuk Rho:** Writing – review & editing, Validation, Supervision, Resources, Project administration, Funding acquisition, Conceptualization.

Declaration of competing interest

The authors declare that they have no known competing financial interests or personal relationships that could have appeared to influence the work reported in this paper.

Appendix A. Supplementary data

Supplementary data to this article can be found online at https://doi.org/10.1016/j.solmat.2024.112848.

References

[1] L.W. Davis, P.J. Gertler, Contribution of air conditioning adoption to future energy use under global warming, Proc. Natl. Acad. Sci. U. S. A. 112 (2015) 5962–5967, https://doi.org/10.1073/PNAS.1423558112/-/DCSUPPLEMENTAL.

[2] L. Pérez-Lombard, J. Ortiz, C. Pout, A review on buildings energy consumption information, Energy Build. 40 (2008) 394–398, https://doi.org/10.1016/j.enbuild.2007.03.007.

[3] Y. Jin, Y. Jeong, K. Yu, Infrared-reflective transparent hyperbolic metamaterials for use in radiative cooling windows, Adv. Funct. Mater. 33 (2023) 2207940, https://doi.org/10.1002/adfm.202207940.

[4] D. Lee, M. Go, S. Son, M. Kim, T. Badloe, H. Lee, J.K. Kim, J. Rho, Sub-ambient daytime radiative cooling by silica-coated porous anodic aluminum oxide, Nano Energy 79 (2021) 105426, https://doi.org/10.1016/j.nanoen.2020.105426.

[5] J. Yun, D. Chae, S. So, H. Lim, J. Noh, J. Park, N. Kim, C. Park, H. Lee, J. Rho, Optimally designed multimaterial microparticle–polymer composite paints for passive daytime radiative cooling, ACS Photonics 10 (2023) 2608–2617, https://doi.org/10.1021/acsphotonics.3c00339.

[6] S. Fan, W. Li, Photonics and thermodynamics concepts in radiative cooling, Nat. Photon. 16 (2022) 182–190, https://doi.org/10.1038/s41566-021-00921-9.

[7] X. Li, B. Sun, C. Sui, A. Nandi, H. Fang, Y. Peng, G. Tan, P.-C. Hsu, Integration of daytime radiative cooling and solar heating for year-round energy saving in buildings, Nat. Commun. 11 (2020) 6101, https://doi.org/10.1038/s41467-020-19790-x.

[8] A.P. Raman, M.A. Anoma, L. Zhu, E. Rephaeli, S. Fan, Passive radiative cooling below ambient air temperature under direct sunlight, Nature 515 (2014) 540–544, https://doi.org/10.1038/nature13883.

[9] B. Ko, D. Lee, T. Badloe, J. Rho, Metamaterial-based radiative cooling: towards energy-free all-day cooling, Energies 12 (2018) 89, https://doi.org/10.3390/en12010089.

[10] S. So, J. Yun, B. Ko, D. Lee, M. Kim, J. Noh, C. Park, J. Park, J. Rho, Radiative cooling for energy sustainability: from fundamentals to fabrication methods toward commercialization, Adv. Sci. 11 (2024) 2305067, https://doi.org/10.1002/advs.202305067.

[11] P. Liu, S. Bae, J. Noh, M. Kim, J.W. Heo, D. Son, J. Kang, J. Rho, S. So, J.G. Kang, I.S. Kim, Functional radiative cooling: basic concepts, materials, and best practices in measurements, ACS Appl. Electron. Mater. 5 (2023) 5755–5776, https://doi.org/10.1021/ACSAELM.3C01023.

[12] MdM. Hossain, M. Gu, Radiative cooling: principles, progress, and potentials, Adv. Sci. 3 (2016), https://doi.org/10.1002/advs.201500360.

[13] J. Li, Y. Fu, J. Zhou, K. Yao, X. Ma, S. Gao, Z. Wang, J.-G. Dai, D. Lei, X. Yu, Ultrathin, soft, radiative cooling interfaces for advanced thermal management in skin electronics, Sci. Adv. 9 (2023) eadg1837, https://doi.org/10.1126/sciadv.adg1837.

[14] S. Byun, J.H. Yun, S. Heo, C. Shi, G.J. Lee, K. Agno, K. Jang, J. Xiao, Y.M. Song, J. Jeong, Self-cooling gallium-based transformative electronics with a radiative cooler for reliable stiffness tuning in outdoor use, Adv. Sci. 9 (2022) 2202549, https://doi.org/10.1002/advs.202202549.

[15] L. Zhu, A. Raman, K.X. Wang, M.A. Anoma, S. Fan, Radiative cooling of solar cells, Optica 1 (2014) 32, https://doi.org/10.1364/OPTICA.1.000032.

[16] E. Akerboom, T. Veeken, C. Hecker, J. van de Groep, A. Polman, Passive radiative cooling of silicon solar modules with photonic silica microcylinders, ACS Photonics 9 (2022) 3831–3840, https://doi.org/10.1021/acsphotonics.2c01389.

[17] M. Kim, D. Lee, S. Son, Y. Yang, H. Lee, J. Rho, Visibly transparent radiative cooler under direct sunlight, Adv. Opt. Mater. 9 (2021) 2002226, https://doi.org/10.1002/adom.202002226.

[18] J. Kim, S. Baek, J.Y. Park, K.H. Kim, J. Lee, Photonic multilayer structure induced high near-infrared (NIR) blockage as energy-saving window, Small 17 (2021) 2100654, https://doi.org/10.1002/smll.202100654.

[19] B. Xie, Y. Liu, W. Xi, R. Hu, Colored radiative cooling: progress and prospects, Mater. Today Energy 34 (2023) 101302, https://doi.org/10.1016/j.mtener.2023.101302.

[20] S. Son, S. Jeon, D. Chae, S.Y. Lee, Y. Liu, H. Lim, S.J. Oh, H. Lee, Colored emitters with silica-embedded perovskite nanocrystals for efficient daytime radiative cooling, Nano Energy 79 (2021) 105461, https://doi.org/10.1016/j.nanoen.2020.105461.

[21] T.Y. Yoon, S. Son, S. Min, D. Chae, H.Y. Woo, J.-Y. Chae, H. Lim, J. Shin, T. Paik, H. Lee, Colloidal deposition of colored daytime radiative cooling films using nanoparticle-based inks, Mater Today Phys 21 (2021) 100510, https://doi.org/10.1016/j.mtphys.2021.100510.

[22] S. Min, S. Jeon, K. Yun, J. Shin, All-color sub-ambient radiative cooling based on photoluminescence, ACS Photonics 9 (2022) 1196–1205, https://doi.org/10.1021/acsphotonics.1c01648.

[23] C. Sheng, Y. An, J. Du, X. Li, Colored radiative cooler under optical Tamm resonance, ACS Photonics 6 (2019) 2545–2552, https://doi.org/10.1021/acsphotonics.9b01005.

[24] E. Blandre, R.A. Yalçin, K. Joulain, J. Drévillon, Microstructured surfaces for colored and non-colored sky radiative cooling, Opt Express 28 (2020) 29703, https://doi.org/10.1364/OE.401368.

[25] G. Ju Lee, Y. Jae Kim, H. Myung Kim, Y. Jin Yoo, Y. Min Song, G.J. Lee, Y.J. Kim, H.M. Kim, Y.J. Yoo, Y.M. Song, Colored, daytime radiative coolers with thin-film resonators for aesthetic purposes, Adv. Opt. Mater. 6 (2018) 1800707, https://doi.org/10.1002/ADOM.201800707.

[26] S. Li, K. Liu, X. Long, L. Chen, Z. Xie, L. Li, X. Zhou, Numerical study of infrared broadband multilayer film absorber with tunable structural colors, Opt Commun. 459 (2020) 124950, https://doi.org/10.1016/J.OPTCOM.2019.124950.

[27] S. So, Y. Yang, S. Son, D. Lee, D. Chae, H. Lee, J. Rho, Highly suppressed solar absorption in a daytime radiative cooler designed by genetic algorithm, Nanophotonics 11 (2022) 2107–2115, https://doi.org/10.1515/NANOPH-2021-0436/MACHINEREADABLECITATION/RIS.

[28] S. So, D. Lee, T. Badloe, J. Rho, Inverse design of ultra-narrowband selective thermal emitters designed by artificial neural networks, Opt. Mater. Express 11 (2021) 1863, https://doi.org/10.1364/OME.430306.

[29] C. Yeung, J.-M. Tsai, B. King, B. Pham, D. Ho, J. Liang, M.W. Knight, A.P. Raman, Multiplexed supercell metasurface design and optimization with tandem residual networks, Nanophotonics 10 (2021) 1133–1143, https://doi.org/10.1515/nanoph-2020-0549.

[30] S. So, T. Badloe, J. Noh, J. Bravo-Abad, J. Rho, Deep learning enabled inverse design in nanophotonics, Nanophotonics 9 (2020) 1041–1057, https://doi.org/10.1515/nanoph-2019-0474.

[31] C. Lee, S. Lee, J. Seong, D.Y. Park, J. Rho, Inverse-designed metasurfaces for highly saturated transmissive colors, J. Opt. Soc. Am. B 41 (2024) 151, https://doi.org/10.1364/JOSAB.505444.

[32] S. Lee, C. Park, J. Rho, Mapping information and light: trends of AI-enabled metaphotonics, Curr. Opin. Solid State Mater. Sci. 29 (2024) 101144, https://doi.org/10.1016/j.cossms.2024.101144.

[33] Q. Guan, A. Raza, S.S. Mao, L.F. Vega, T. Zhang, Machine learning-enabled inverse design of radiative cooling film with on-demand transmissive color, ACS Photonics 10 (2023) 715–726, https://doi.org/10.1021/acsphotonics.2c01857.

[34] Y. Liu, X. Weng, P. Zhang, W. Li, Y. Gong, L. Zhang, P. Zhou, L. Deng, Broadband absorption of infrared dielectric resonators for passive radiative cooling, J. Opt. 23 (2021) 025102, https://doi.org/10.1088/2040-8986/abd4bf.

[35] W. Ma, W. Chen, D. Li, Y. Liu, J. Yin, C. Tu, Y. Xia, G. Shen, P. Zhou, L. Deng, L. Zhang, Deep learning empowering design for selective solar absorber, Nanophotonics 12 (2023) 3589–3601, https://doi.org/10.1515/NANOPH-2023-0291/MACHINEREADABLECITATION/RIS.

[36] C. Xie, H. Li, C. Cui, H. Lei, Y. Sun, C. Zhang, Y. Zhang, H. Dong, L. Zhang, Deep learning assisted inverse design of metamaterial microwave absorber, Appl. Phys. Lett. 123 (2023) 181701, https://doi.org/10.1063/5.0171437/2919094.

[37] S. Jeon, J. Shin, Ideal spectral emissivity for radiative cooling of earthbound objects, Sci. Rep. 10 (2020) 13038, https://doi.org/10.1038/s41598-020-70105-y.